JOURNAL OF THERMOPHYSICS AND HEAT TRANSFER
Vol. 11, No. 4, October–December 1997

Computations of High-Speed, High Knudsen Number Microchannel Flows

C. K. Oh,* E. S. Oran,† and R. S. Sinkovits‡
U.S. Naval Research Laboratory, Washington, D.C. 20375-5344

The effect of varying the Knudsen number *Kn* in microchannel flows was simulated using the direct simulation Monte Carlo method (DSMC) combined with the monotonic Lagrangian grid (MLG). The DSMC–MLG, a method that provides automatic grid refinement according to number density, has been optimized for massively parallel computation and provides a fast, highly resolved description of the flow. New outflow boundary conditions, consistent with the DSMC–MLG algorithm, were developed to allow the user to specify the outflow pressures. The effect of varying *Kn* was examined for three different values of *Kn* (0.07, 0.14, and 0.19) for a high-speed inflow by varying the channel height. A Navier–Stokes computation was also performed to show continuum regime flow. The computations provide contours of pressure, temperature, and Mach number to show complex interactions among oblique shocks and boundary layers, and how these change with the *Kn*. Temperature jumps and slip velocities as functions of position along the wall are compared for all cases. The computations show that the velocity slip is approximately constant behind the shock, while the temperature jump is reduced.

Nomenclature

i, j = grid indices
L = characteristic length
N = data structure
s = second
T = temperature, K
u = streamwise velocity, cm/s
V = velocity
x, y = Cartesian coordinate
$\boldsymbol{\lambda}$ = mean free path

Subscripts
f = fluid
th = thermal
x, y = Cartesian coordinate
∞ = freestream

Introduction

MICROMINIATURIZATION of devices, such as microactuators, microrefrigerators, and microgenerators,[1,2] has become important because of their applications to medical and engineering problems.[3,4] Combining these micromechanical systems with electronic sensors could result in controllable integrated systems. The success of designing and fabricating these devices depends on the operation of a number of components, the most fundamental of which are flows through narrow microchannels with dimensions ranging from tenths to hundreds of microns. Thus, understanding and using the physics of such flows is essential in developing micro–electro–mechanical systems (MEMS). There are still many questions to be answered on the observed behavior of MEMS flows, even for simple planar microchannels.

Received March 31, 1997; revision received May 19, 1997; accepted for publication May 20, 1997. This paper is declared a work of the U.S. Government and is not subject to copyright protection in the United States.

*Research Aerospace Engineer, Laboratory for Computational Physics and Fluid Dynamics. Member AIAA.

†Senior Scientist for Reactive Flow Physics, Laboratory for Computational Physics and Fluid Dynamics. Fellow AIAA.

‡Research Physicist, Laboratory for Computational Physics and Fluid Dynamics; currently at San Diego Supercomputer Center, San Diego, CA 92186-5608.

In many microchannel systems, the mean free path of the molecules is of the order of the system size. In these cases, the Knudsen number $Kn = \boldsymbol{\lambda}/L$, where λ is the mean free path of the gas molecules and L is a characteristic length of flow gradient in the system, is in a rarefied gas flow regime ($0.01 < Kn < 10$). In this regime, many concepts from continuum dynamics do not apply, and molecular-level kinetics must be explicitly considered. Because of the small dimensions of many microchannels, the Reynolds number is extremely low ($\sim$10), which means that the viscous forces are comparable to the inertial forces. Therefore, viscous momentum transport from the wall to the flow is a very important aspect of the microchannel flow. In addition, the behavior of the fluid near the walls is poorly understood. Rough surfaces and high gradients in the fluid variables, such as velocity and pressure, may affect transport in ways different from those in larger systems. These boundary-layer effects may lead to Knudsen numbers that are even higher than the bulk-flow estimates.

Bulk micromachining technology has been used to make microchannels with precise dimensions.[5,6] Using such channels, measurements of the pressure differences across the channels and the flow rates for very low-velocity flows[6–8] show that there are definite differences between continuum predictions and the experiments. The small size of the microchannels results in high *Kn* and failure of the traditional continuum scaling laws.

The direct simulation Monte Carlo method (DSMC) is a well-established method for modeling flows for which $Kn > 0.1$.[9] It can be used to describe two very different physical situations that produce large values of *Kn*. For rarefied gasdynamics characterized by high-altitude flows, the mean-free-path of the particle is large and the density is low. In the last few years, DSMC has been extensively used for studying such problems as the flows around the Space Shuttle orbiter[10] at altitudes of 100 km. For microchannel flows, *Kn* is large because the dimensions of the channel are small. The DSMC has only recently been used to simulate flows in microdevices.[11,12]

A conventional DSMC approach involves tracking the trajectories of simulated particles on a fixed spatial grid that defines the spatial cells. In an effort to automatically adapt the grid to account for changing flow properties, a new technique based on a monotonic Lagrangian grid (MLG) has been developed.[13] The MLG is a general data structure in which the nodes can represent particles. The MLG ensures that particles

close in physical space are close in computer memory. Using the MLG data structure, physical space is divided into a number of templates (cells), each containing the same number of particles. Recently, the DSMC and MLG were combined to produce a method with automatic grid adaptation based on changes in basic flow properties.[13] This automatic grid adaptivity is extremely useful when there are evolving or unforeseen steep gradients.[13,14] This method has also been parallelized and optimized to produce a fast and efficient code for treating very large numbers of particles, so that the properties of more realistic and larger systems can be accurately computed.[15]

In material processing, various DSMC boundary conditions such as a vacuum pump rate boundary condition and variable porosity wall boundary conditions have been developed.[16,17] However, in most rarefied hypersonic channel-flow simulations,[18,19] the vacuum condition is used as an outflow boundary condition. Yasuhara et al.[18] tested a mirror image supersonic outflow boundary condition proposed by Vogenitz et al.[20] Comparisons to computations using the vacuum boundary condition showed that there was a significant difference between the two boundary conditions. However, the boundary condition of Vogenitz et al.[20] was applicable to the flows that have no streamwise gradient. For microchannel flows operating at atmospheric conditions at the outflow, feedback from outside the computational domain may be substantial and vacuum boundary conditions give erroneous results. Recently, characteristic[21] and imposed pressure boundary conditions[12] have been developed for MEMS flows in nonvacuum boundary conditions.

This paper presents results of a study of high Kn microchannel flows at pressures above atmospheric. We first present an analysis that shows that it is impractical to simulate high-pressure flows for which the ratio between the fluid velocity V_f and molecular thermal velocity V_{th} is very small. The limitation on the computation arises because of the monumentally large number of small timesteps and the significant number of ensembles that are required to eliminate the effects of statistical fluctuations. Then, the effect of varying Kn is examined for three different values of Kn for a high-speed inflow by varying channel height. To our knowledge, there has been no consistent documentation in the literature on how a channel flow varies as Kn goes from low (0.01) to fairly high (0.2) values. A new outflow boundary condition was developed to accommodate the subsonic outflow conditions that are needed in this study.

Method

The MLG is a general data structure for organizing and sorting data in any number of dimensions.[22] In the problem described here, we have two-dimensional data structure. The location of each node in the MLG data structure is determined by the set of constraints:

$$\begin{aligned} x(i,j) &\le x(i+1,j) \quad \text{for} \quad 1 \le i \le N_x - 1, \quad \text{all} \quad j \\ y(i,j) &\le y(i,j+1) \quad \text{for} \quad 1 \le j \le N_y - 1, \quad \text{all} \quad i \end{aligned} \tag{1}$$

where the set (N_x, N_y) defines the data structure, and (i, j) represents the grid indices in the x and y directions. Particle positions are swapped in memory to achieve and then maintain this MLG order. Once the nodes are sorted into MLG order, the interactions between nearby nodes are found by searching through index space rather than physical space. For example, the neighbors of a particle stored at the location (i, j) in a two-dimensional array can be found by searching the neighboring array locations $(i + 1, j)$, $(i + 1, j + 1)$, $(i, j + 1)$, etc. The MLG conditions defined by Eq. (1) are not sufficient to define a unique order for the particles within the data structure. Recent studies by Sinkovits et al.,[23] addressing issues involved in constructing an MLG with the best properties, determined that the best quality MLGs are, in fact, the easiest to obtain. The MLG has been used previously in molecular dynamics[24] calculation, and recently, Cybyk[13] has shown that it can be combined with DSMC.

It is possible to abandon the fixed spatial grid in a conventional DSMC calculation by using the MLG. Particle templates are defined by groups of the particles that are subdivided into the nearest-neighboring blocks containing equal numbers of particles. Therefore, the locations of the particles are then used to define the boundaries of the templates. In contrast to conventional DSMC, each template in the DSMC–MLG is formed by defining a group containing the same number of particles. The result is that the template grid automatically adapts to account for the local changes in number density in the system.

The grid can become very distorted in regions of high molecular concentrations and extremely large gradients. This can result in a nonphysical situation in which collisions between spatially close particles are ignored while interactions between more widely separated particles are considered. In addition, the irregular shapes of the highly skewed templates in the distorted region of the grid can lead to errors in the evaluation of the template areas.[13] To minimize these problems, a grid-restructuring technique, stochastic grid regularization[23] (SGR) is employed. In applying SGR, the following additional steps are taken. The particles that have been put in MLG order are randomly displaced in space, and the data are swapped until monotonicity conditions are satisfied for the perturbed node positions. Finally, data are swapped until the monotonicity conditions are satisfied for unperturbed node positions. A detailed study performed to determine the optimal SGR parameters for a hypersonic wedge flow shows that the grid gives the most accurate results when it adapts to the flow structure.[15]

Use of the massively parallel Connection Machine has allowed us to perform more resolved and longer computations.[15] The DSMC–MLG parallelization is performed on two different levels. First, simulated particles are mapped onto processors, and then particle templates are mapped separately onto the processors. Communication between the two levels is optimized. In addition, a method to improve load-balancing was developed, which also has the benefit of decreasing required computer memory. The most intensive communication between the particle and template arrays takes place during the calculation of binary collision. Calculating binary collisions at the particle level is inefficient because it leads to a situation where the majority of the processors are idle, and thus, to a load-balancing problem. In the parallelization technique used here, a collision pair is chosen randomly at the particle level and then interprocessor communications are used to transfer the data for the pair from the particle arrays to the template arrays. All operations are then carried out at the template level, and the results after the collisions are then communicated back to these particle arrays. These procedures are repeated until each template satisfies the requirements set by the no time counter (NTC)[9] collision method at each timestep. All independent particles in each template participate in the collision process. This means that the parallel collision method preserves the statistical independence in selecting collision pairs. As a result, the remapping converts global communications between particles into the local communications between particles in each template.

The parallel efficiency, defined as the increase in computing speed divided by the number of processors used, was measured for computations based on 51,200, 132,072, and 528,288 simulated particles.[15] For the calculations done using 51,200 particles, the parallel efficiency is poor, dropping below 40% at 512 processors. However, the efficiency increases as the number of simulated particles and templates increases. With 528,288 particles, the efficiency reaches approximately 80%. Computing time required by the parallel DSMC–MLG code was significantly decreased compared to other parallel efforts. For more detailed information on the parallelization, refer to Oh et al.[15]

The Rayleigh problems[9] has been used as a standard problem for validating DSMC codes. The DSMC one-dimensional solutions of this problem have been validated by comparing to both Bhatnagar, Gross, and Krook (BGK) and analytical solutions. This Rayleigh problem was used to test two-dimensional versions of the parallelized DSMC–MLG.[15] Also, extensive tests of resolution and sample size were performed for the hypersonic, high-Kn flow in the channel–wedge configuration.[14]

Problems for Computing Low-Speed Microchannel Flows

The most comprehensive experimental study of microchannel flows has been performed by Pong et al.,[7] using He and N_2 gases. Typical channel dimensions are 1.2 μm high by 5 μm wide by 3000 μm long. The undisturbed gas pressure and temperature are 1 atm and 298 K, respectively, and the inflow velocity is approximately 20 cm/s.

Timesteps and Resolution Limitation

Because the number density at 1 atm is so much higher than that of any rarefied pressure condition, the mean collision time is very small, of order of 10^{-10} s. In DSMC, the computational timestep[9] must be less than the mean collision time. The particle transit time, which is the time that a flow with speed 20 cm/s takes to pass through the channel, is 10^{-2} s. Therefore, the minimum number of timesteps to reach the steady-state flow condition requires 10^8 timesteps. Such a calculation would be well beyond the capabilities of current computers.

A full three-dimensional simulation of the experiments would also be impractical because of the large number of computational cells required. One of the conditions that must be satisfied during a DSMC procedure is that the smallest dimensions of the computational cells must not be greater than one-half of the mean free path. For the microchannel described earlier, a minimum of 500,000 cells would then be required.

Statistical Scatter

The importance of statistical scatter caused by small perturbations increases as the flow velocity becomes subsonic, so that $V_f << V_{th}$. For the present problem, the thermal speed is approximately 1000 m/s. With the 0.2-m/s flow speed mentioned earlier, the statistical noise is four orders of magnitude greater than the required signal. Therefore, a disturbance in such a low speed can be completely lost in the noise. However, as the sample size from either the ensemble or time average increases, the correct result will, in principle, emerge. The solution of a microchannel flow at 0.2 m/s would require over 10^8 samples in a time-averaged steady flow because the statistical fluctuations decrease with the square root of the sample size. This statistical scatter is considered in addition to the intrinsic statistical scatter in the DSMC method. This intrinsic scatter arises because DSMC represents an extremely large number of real molecules by a relatively small number of simulated particles. Reducing these sources of scatter to produce a reliable solution is beyond the capability of current computers, and the large number of timesteps that would be required to reach steady flow in the large systems may pose an even more difficult problem. Generally, in the DSMC framework, the flows with high velocities are much easier to compute than flows with low velocity.

The conclusion is that we cannot accurately simulate a 3000-μm channel where the gas is moving at very low subsonic flow velocities and the freestream pressure is 1 atm or greater. Therefore, we begin this study with simulations of high Mach number microchannel flows, for which the velocities are of the same order of magnitude as molecular thermal velocity, and for much smaller systems.

Computational Domain and Flow Conditions

Figure 1 illustrates the computational domain and wall boundary conditions for the high-speed microchannel flow simulation. For the standard test case, the computational domain consists of a rectangular channel, 6 μm long by 1.2 μm high, filled with He gas. There is a freestream section 1 μm long upstream of the leading edges of the channel. The undisturbed pressure and temperature are 1 atm and 298 K, respectively.

The variation in Kn was achieved by varying the channel height, while keeping the ratio of channel height to length constant. The freestream Mach number of the flow entering the channels is the same for all three cases, $M_\infty = 5$. Geometric properties and flow conditions are given in Table 1. The lowest value of $Kn = 0.07$ (case 1) is close to the continuum regime, and $Kn = 0.14$ and 0.19 (cases 2 and 3) are in the transitional regime. The local Kn, defined earlier in the introduction section, was also calculated for three different cases. The minimum, maximum, and averaged values for cases 1, 2, and 3 are shown in Table 2.

At the start of a calculation, all particles are initialized with the same value of the streamwise velocity. The channel surfaces are kept at the freestream temperature 298 K. Two sets of computations were performed, one using the hard sphere (HS) collision model and another using the variable hard sphere (VHS) collision model. All of the results presented here are for the VHS model. The convection timestep is 10% of the mean collision time of the undisturbed gas.

The upper and lower boundaries in the region $0 \leq x \leq 1$ μm (drawn as thinner horizontal boundary lines in Fig. 1), which is the region just before the channel walls begin, are modeled using a specularly reflecting boundary condition. This means that the molecular velocity component normal to the surface is reversed during the interaction, while the component to the surface remains unchanged. The use of the specular boundary condition prevents the disturbance from affecting the upstream boundary. We refer to the conditions in this regime as the uniform freestream flow condition of the problem. The upper and lower wall boundary conditions are fully diffuse, which means that the velocity of each molecule after reflection from the walls is randomly determined from the appropriate thermal distribution. The temperature of the wall determines the appropriate thermal distribution to use.

When using the inflow-outflow boundary condition developed by Cybyk,[13] the length of the computational domain is not fixed. Particles leaving index space at the outflow were reused in the simulation by reintroducing them again at the inflow with the appropriate inflow conditions. In this study, the fixed-length inflow-outflow condition that Nguyen et al.[14] developed was used. The idea for maintaining this constant-length boundary is that the boundary condition is applied in physical space rather than in index space.

An outflow boundary condition is used that accounts for finite pressures outside the computational domain. This is done by defining a virtual (or ghost) region outside of the computational domain, drawn by the dotted lines in Fig. 2. Virtual particles, represented by white circles, are distributed through this region. These particles do not move during the computation. Thus, there are no interactions between particles and walls. However, the templates, represented here by polygons, are composed of both virtual and real particles. For example, Fig. 2 shows templates formed by 3 × 3 particles. By speci-

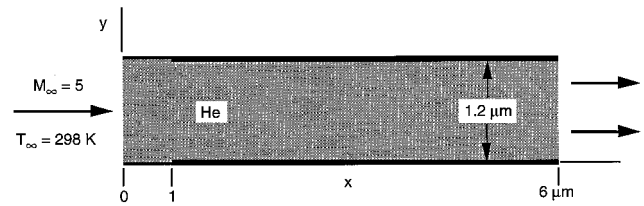

Fig. 1 Schematic for the microchannel flow simulations: ——, freestream section and specular surface; ▬▬, wall condition and fully diffuse.

Table 1 Flow conditions for the microchannel simulations

Quantity	Case 1	Case 2	Case 3
x_{max}, μm	12	6	4.4
y_{max}, μm	2.4	1.2	0.88
Freestream distance, μm	2	1	0.73
Kn	0.07	0.14	0.19
Number of templates	3,712	928	928
Number of particles per template	6×6	7×7	7×7
Total number of particles	133,632	45,472	45,472
M_∞	——	5.0	——
Number density, cm^{-3}	——	2.456×10^{19}	——
T_∞, K	——	298	——
Mean free path for undisturbed gas, cm	——	0.169×10^{-4}	——
Undisturbed gas pressure, dyne/cm^2	——	1.01×10^6	——

Table 2 Values of maximum, minimum, and averaged local Kn for cases 1, 2, and 3

Local Kn	Case 1	Case 2	Case 3
Minimum value	0.0004	0.0043	0.0045
Maximum value	1.47	1.64	7.2
Averaged value	0.19	0.21	0.49

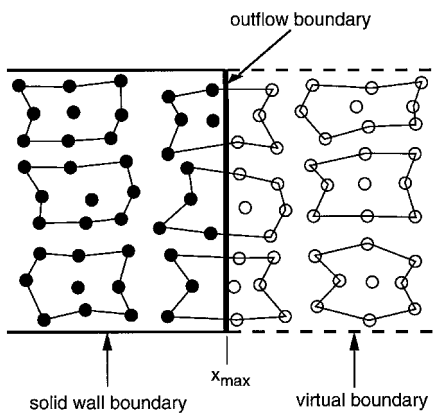

Fig. 2 Outflow boundary treatment using virtual templates and particles; black and white circles are real and virtual particles, respectively.

fying an exit backpressure in the virtual region, the area of each template that includes any virtual particles (therefore, including mixed templates) is updated according to the equation of state. Therefore, the areas of the virtual templates are continually changed by this imposed pressure. These updated template areas are used in the collision process. The possible number of collision pairs for each template is changed as a function of template area. This means that outflow boundary information represented by backpressure is transmitted by intermolecular collisions. Therefore, the outflow boundary, shown by the thick vertical line at $x = x_{max}$, should intersect the boundaries of templates. The collision velocities of virtual particles are set by copying the velocities of real particles close to x_{max} onto the virtual particles. This can be done because the velocities of virtual particles are almost the same as the velocities of particles close to the outflow boundary. These velocities are for computational purpose only. These outflow boundary conditions, which are consistent with the DSMC–MLG algorithm, can prescribe the outflow backpressures.

High-Speed Microchannel Flow

Figures 3a–3c show the computational grids for cases 1–3, respectively, after the flows have reached a steady state. The intersections of the grid lines indicate the locations of the centers of mass of the templates. For a reasonably accurate DSMC computation, the computational cell size should be half of the mean free path.[9] In the present computations, the freestream mean free path is constant for all three cases; therefore, Kn is function of the channel height. The number of cells for case 1 (near-continuum regime) was doubled in each direction compared to that for cases 2 and 3 (transitional regime). The horizontal and vertical axes of a microchannel are normalized by the maximum channel height. Because the aspect ratio of the channel height and length remained constant for all three cases, the normalized x and y dimensions are the same.

Initially, the grid is uniform for all three cases. However, as the flow evolves, it changes dynamically in response to changes in the local particle density. All three grids are nearly uniform in the freestream section ($0 < x < 0.8$), then adapt according to the incident oblique shocks emanating from the leading edges of the channels ($x = 0.8$). Comparing Fig. 3 to contours of pressure and Mach number (Figs. 4 and 5) shows that the different grids have adapted according to the angles and strengths of the oblique shocks. The grids for all cases are less skewed downstream where the flow is relatively smooth. This grid adaptation, which produces more accurate solutions for a given grid resolution, is a property of the DSMC–MLG approach. After the flow reached steady state, the next 500 timesteps were used to compute time-averaged solutions. The statistical scatter is reduced through this time-average procedure.

Flow Dynamics

Pressure, Mach number, and temperature contours are shown in Figs. 4–6, respectively. The same normalized x- and y-coordinate system was used in Fig. 3.

Pressure contours, shown in Figs. 4a–4c, show how the flow changes with Kn. Figure 4a shows two bow shocks emanating from the leading edges of the microchannel. These two bow shocks intersect at $x \approx 2.0$, and then separate and extend to the walls. The waves resulting from the intersection of the bow shocks are diffuse and the shock reflections from the walls are very weak. The highest pressure appears at the point of shock intersection. This intersection of the bow shocks is not seen for larger values of Kn (Figs. 4b and 4c) because the shocks are even more diffuse and weaker. Figure 4a also shows the strong pressure gradients across the bow shocks near the walls

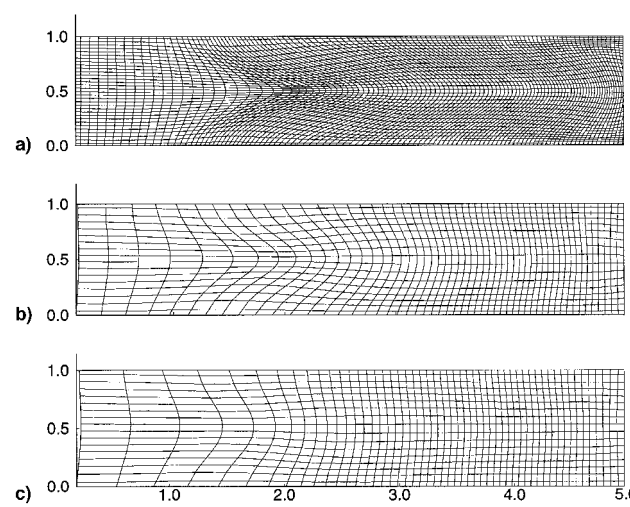

Fig. 3 Computational mesh, as determined by the c.m. of the templates for Kn = a) 0.07, b) 0.14, c) 0.19. The x and y coordinates are normalized by channel height.

of the leading edges. These gradients become weaker away from the walls because the incident shock strength is weakened by the expansion waves at the leading edges,[26] an effect that is consistent with oblique shock theory. The pressure is highest at the center of the computational domain in Fig. 4c, Kn = 0.19, and then it gradually decreases downstream.

Mach number contours are shown in Figs. 5a–5c. As the Kn increases, the leading-edge shocks become thicker and the oblique shock angles measured from channel wall are greater. For Kn = 0.07, the higher Mach number region represented approximately by the M = 3.0 contour, extends far downstream along the channel center. As Kn increases, this region moves upstream, because of the increased importance of viscosity that slows and heats the fluid. Even though the freestream Mach number is the same for all three cases (M_∞ = 5), the Mach number range downstream of the leading oblique shocks varies from supersonic to subsonic. At the outflow boundary, the velocity for Kn = 0.07 is supersonic, except in the vicinity of the walls. However, the flow speed is subsonic at the outflow boundary for the Kn = 0.19 case. These cases again show the necessity of using an outflow boundary condition that can handle both supersonic and subsonic conditions. In front of the leading edges, detached bow shocks are formed because of the viscous boundary layers.[25] At Kn = 0.19, the detachment is most severe and near the wall, and these bow shocks are nearly normal. This is consistent with experimental and theoretical predictions[25] where detached shock waves of a continuum gas are normal to the freestream direction on the axis of symmetry of obstacle.

The growing boundary layer begins to form at the leading edge of the channel. This boundary layer presents a growing wedge to the approaching supersonic flow, which is deflected by the wedge angle. The wedge angle of the Kn = 0.07 case is just over 14 deg (measured from the density contour, not shown here), and the oblique shock angle (also measured from density contour) is about 22 deg. The theoretical oblique shock angle[26] determined for a monatomic gas at this freestream Mach number and wedge angle is 25 deg. This is relatively good agreement, even though the theory is for a continuum case. The boundary layers of Kn = 0.07, originating at the

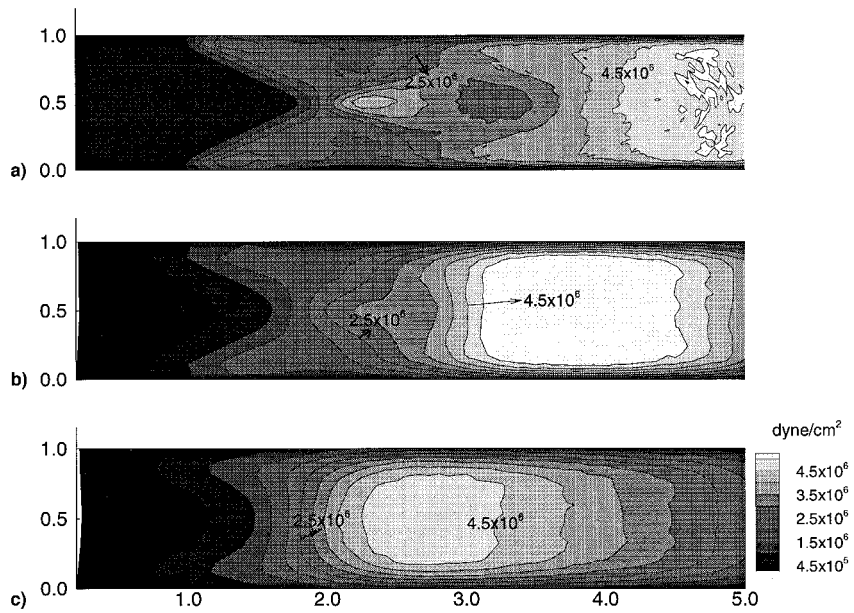

Fig. 4 Pressure contours at steady state. Kn = a) 0.07, b) 0.14, and c) 0.19.

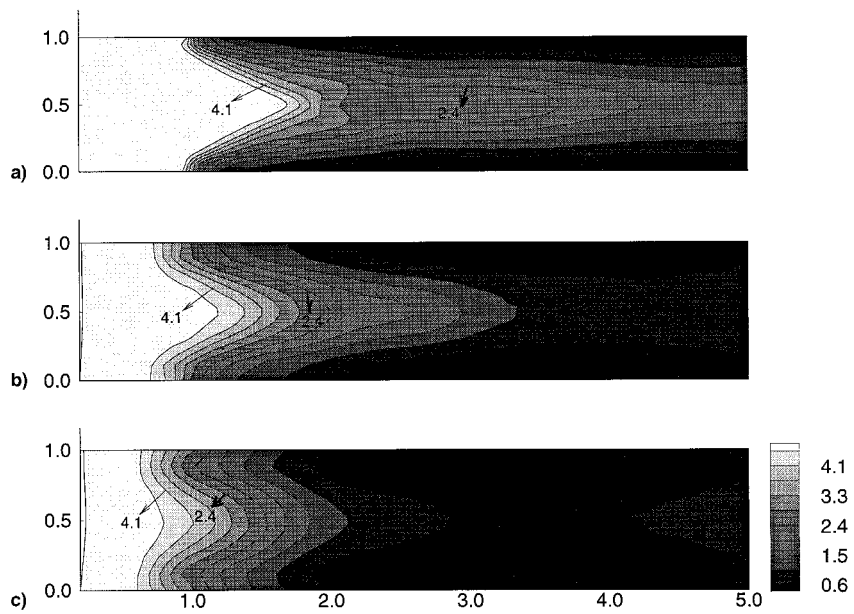

Fig. 5 Mach number contours at steady state, Kn = a) 0.07, b) 0.14, and c) 0.19.

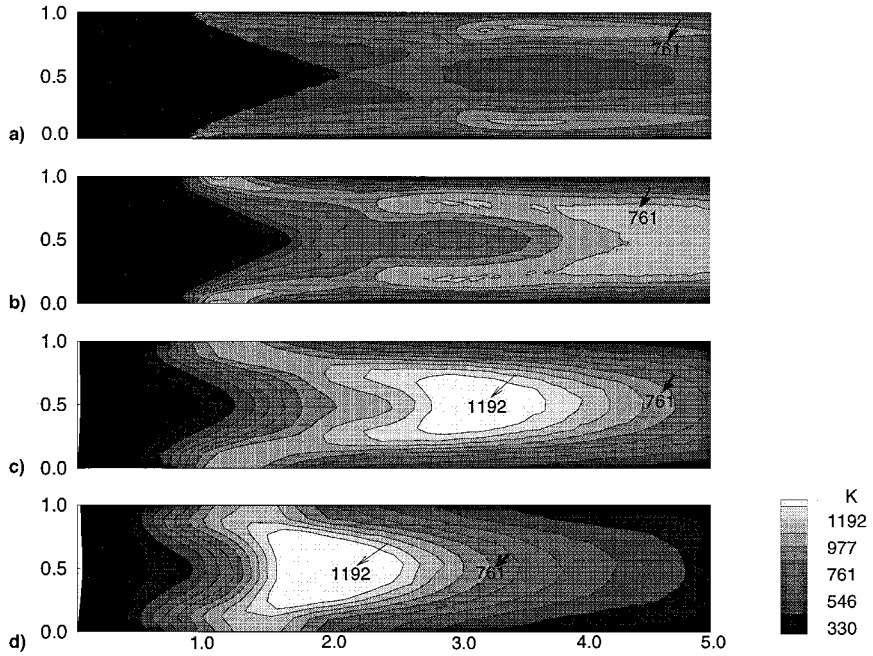

Fig. 6 Temperature contours at steady state. *Kn* = a) 0.01 (NS solution), b) 0.07, c) 0.14, and d) 0.19.

leading edges of the walls, continuously grow up to $x = 2.4$. Then reflected shock waves from the walls (Fig. 4a) suppress the growth of boundary layers. After that, boundary layers again start growing. This boundary-layer growth can be seen after $x = 2.4$ in Fig. 5.

Temperature contours are presented in Fig. 6 along with a comparison of a Navier–Stokes (NS) solution for an essentially continuum case of $Kn = 0.01$ (Fig. 6a) to DSMC–MLG results (Fig. 6b–6d). The NS computations were performed using a parallelized code based on flux-corrected transport (FCT) for convective transport and central-differencing for diffusive transport.[27] In this regime of very small *Kn*, NS computations are much more efficient and faster than DSMC computations. These were performed on a 254×62 uniformly spaced grid with no-slip velocities at the wall. The thickness of thermal boundary layer increases with *Kn*, a trend that is consistent with the behavior of the calculated oblique shock angle and thickness.

Velocity Slip and Temperature Jump

The streamwise velocity and temperature profiles (Figs. 7 and 8) were determined by interpolating from the templates to points on the $x = 0.8$, 1.6, 2.4, 3.2, 4.0, and 4.8 lines. The vertical axis is the normalized y coordinate (y/y_{max}) and the horizontal axis is the magnitude of the variable.

All three cases show a primary peak at the centerline of the streamwise velocity profiles shown in Figs. 7a–7c. The peak values at different downstream stations are relatively constant in the $Kn = 0.07$ profile. However, because of the strong viscous effect, the peak values of $Kn = 0.14$ and 0.19 are significantly reduced as the flow develops downstream. For higher *Kn*, there is more slip near the channel entrance. In particular, consider $x = 1.6$. At this location, the velocity slip increases by almost a factor of 2 from $Kn = 0.07$ to 0.14, and only slightly from $Kn = 0.14$ to 0.19. However, the velocity slip at the wall does not change significantly beyond $x = 2.4$ for any case studied.

The temperature profiles along the various x stations, Fig. 8a–8c, show the development of thermal boundary layers. Figure 8a for $Kn = 0.07$ shows twin peaks in all the profiles, then these peaks merge downstream. In this case, the fully developed state is not reached downstream in this calculation. For $Kn = 0.14$, the peaks merge at $x = 3.2$, where the flow reaches a fully developed state. Downstream of this, the peak value of temperature gradually decreases. For $Kn = 0.19$, the fully developed state occurs at $x = 2.4$, and then the peak value at the centerline decreases significantly downstream. In all cases, the temperature jump is largest close to the channel entrance ($x = 1.6$), and the size of jump increases as *Kn* increases. However, the temperature jump is reduced downstream for higher *Kn*.

Viscous Effects

Figures 9 and 10 show the Mach numbers, pressures, temperatures, and densities at the centerline and walls, respectively. The behavior of the variables along the centerline (Fig. 9) can be compared qualitatively with results obtained from the one-dimensional compressible, viscous flow solution in constant-area ducts with friction (Fanno solution[25]). Even though the incoming velocity at the inlet has oblique shocks emanating from the tip of the wall, we can still compare our results downstream of the shocks to the Fanno solution. The Mach number for the flow $Kn = 0.07$ is still supersonic after the shock. Therefore, the Mach number decreases along the channel, but does not reach sonic conditions. The temperature, pressure, and density increase along the channel. These facts are all consistent with the Fanno results. However, for the transitional flow regime ($Kn = 0.14$ and 0.19), the flow becomes subsonic and then the Mach number increases along the downstream direction. The pressure, temperature, and density (Figs. 9b–9d) decrease, which is consistent with the Fanno results.

Figure 10 shows the profiles of Mach number, pressure, temperature, and density at the wall. All three values of *Kn* show similar trends, but the shock thicknesses are different. The shock thickness of $Kn = 0.07$ was measured by using the curvatures of pressure at the wall, where the shock is normal (Figure 10b) based on 95% of the pressure difference across the shock. This was then compared to the approximate numerical prediction of shock-layer thickness solving Boltzmann equation (Mott–Smith solution)[28] for large values of Mach number. In this work, Mott–Smith performed the calculation with a bimodal distribution function that weighted the sum of the upstream and downstream distribution function. The Mott–Smith result showed fairly good agreement with experimental data, particularly for $M_\infty > 4$. The Mott–Smith ratio of the shock thickness to the freestream mean free path for a

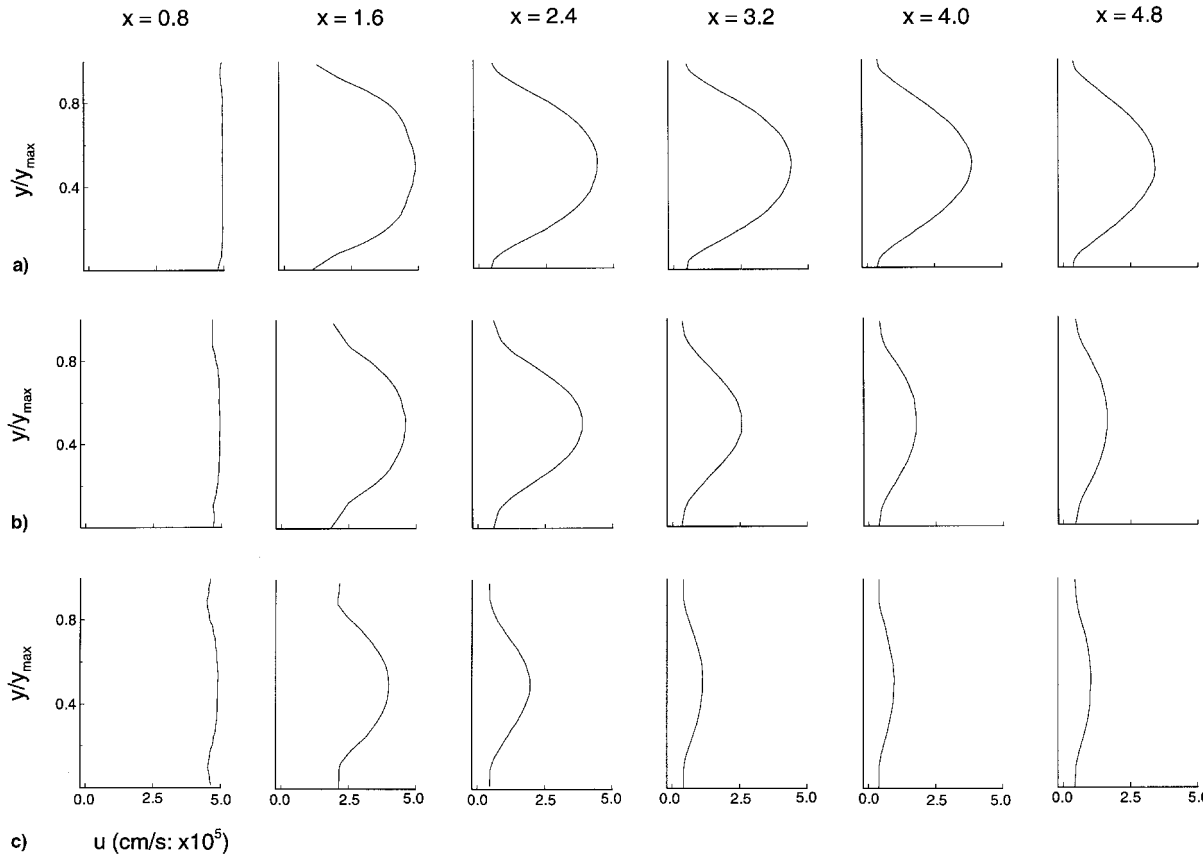

Fig. 7 Streamwise velocity profiles at various normalized x locations along the channel; x = 0.8, 1.6, 2.4, 3.2, 4.0, and 4.8 for different Kn = a) 0.07, b) 0.14, and c) 0.19.

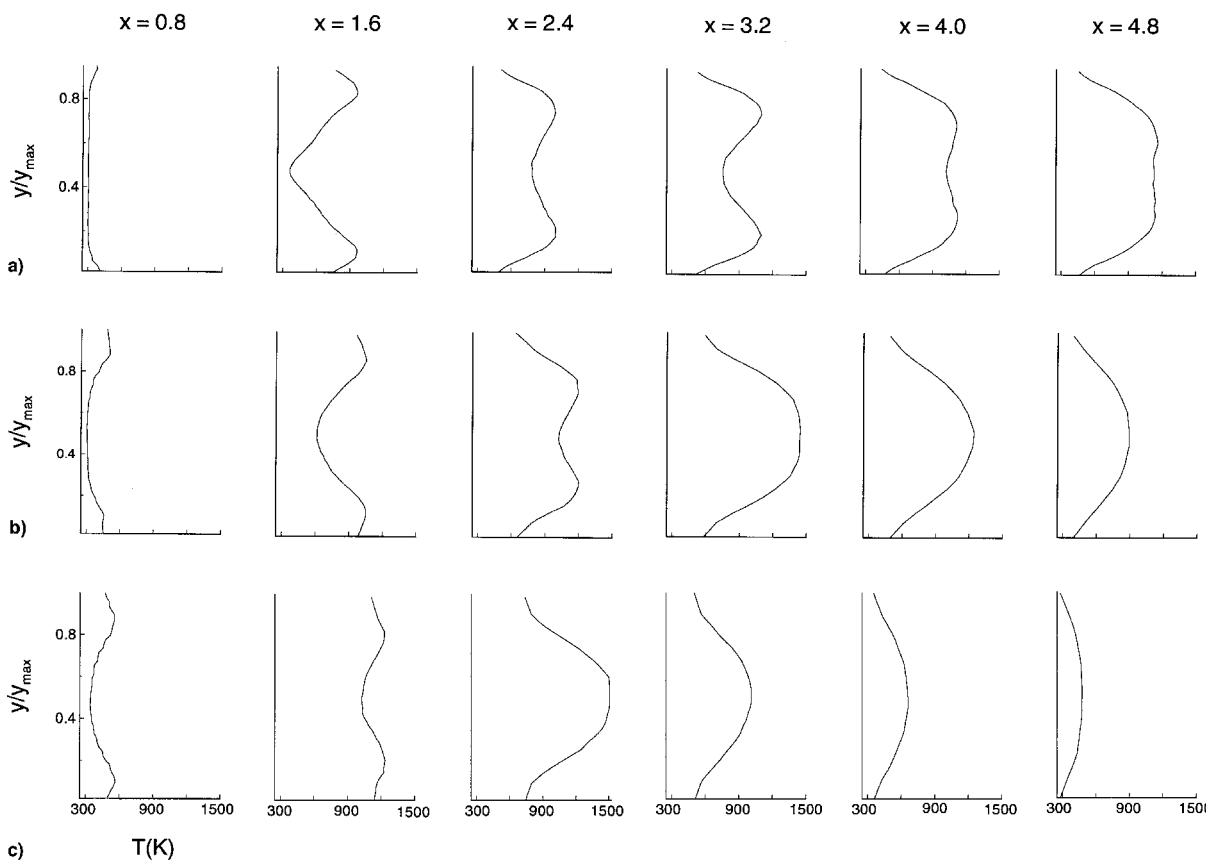

Fig. 8 Temperature profiles at various normalized x locations along the channel; x = 0.8, 1.6, 2.4, 3.2, 4.0, and 4.8 for different Kn = a) 0.07, b) 0.14, and c) 0.19.

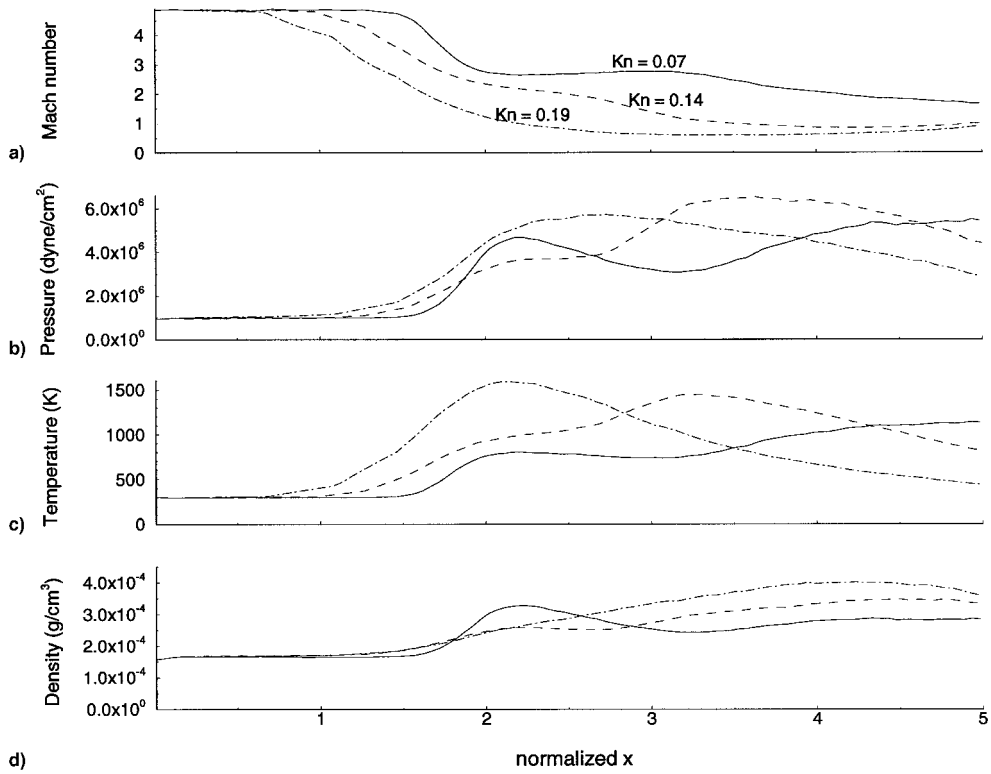

Fig. 9 Centerline (y = 0.5) profiles for different values of Kn: a) Mach number, b) pressure, c) temperature, and d) density.

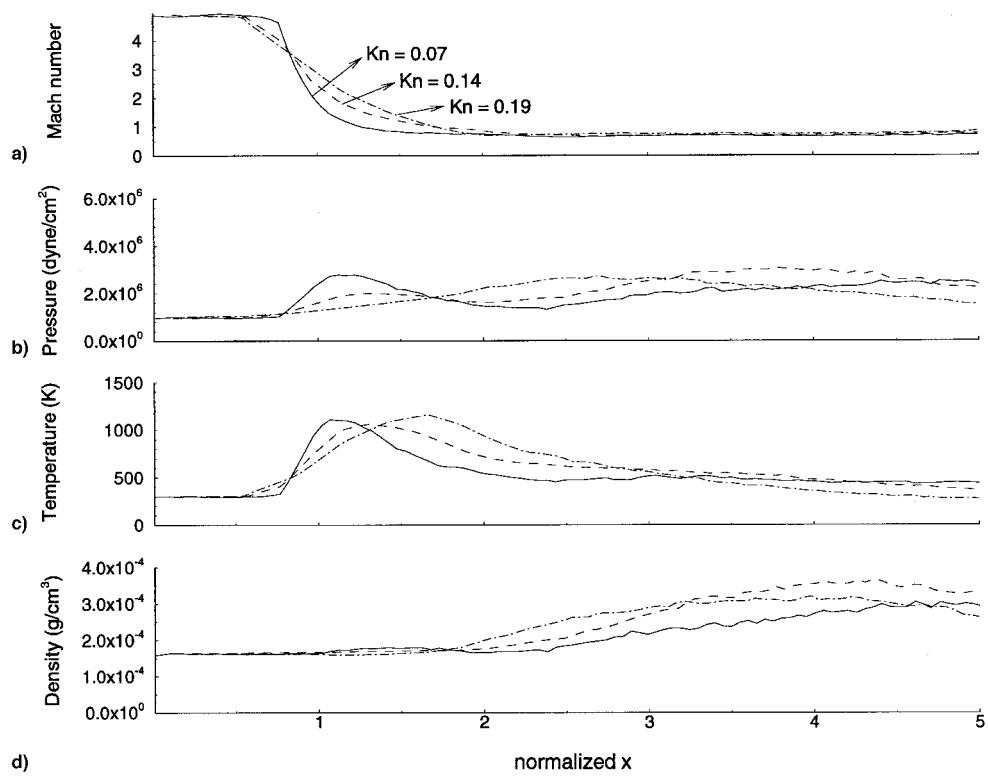

Fig. 10 Wall (y = 0) profiles for different values of Kn: a) Mach number, b) pressure, c) temperature, and d) density.

monatomic gas is 3.4. The value from the present DSMC calculation with the VHS model is about 3.55, and the value obtained from the computations (not shown) using the HS model is 3.8. The differences may come from the way the ratio is determined graphically from the DSMC calculation or the approximate distribution function used in the Mott–Smith solution. Once again, as Kn increases, the shock is thicker.

Conclusions

The massively parallelized DSMC–MLG code was used to study high-speed high Kn microchannel flows. For this problem, a new outflow boundary condition, consistent with DSMC–MLG algorithm, was developed to allow specifying the outflow pressures. An important aspect of obtaining good agreement comes from the adaptive grid system based on local number density.

Low-speed flows in many current experiments are very expensive to simulate by DSMC because the statistical fluctuations are very large when the thermal speeds are much larger than flow speed. Therefore, the present study focused on Kn effects in high-speed flows.

The effect of varying Kn was investigated for a flow of He gas initially at 298 K and 1 atm. Three different values of Kn (0.07, 0.14, and 0.19) were set by varying the channel height, while the aspect ratio between the channel height and length was held constant. A Navier–Stokes computation was also performed to provide the result for a limiting value, $Kn = 0.01$. The $Kn = 0.01$ and 0.07 cases could be considered as continuum and near-continuum flow, and the other two cases are in the transitional regime flow. The downstream development of flow variables qualitatively follows the prediction of the theoretical Fanno prediction. Also, the shock thickness measured in the near-continuum regime agrees fairly well with the numerical prediction obtained solving the Boltzmann equation. Given the flow deflection angle, the oblique shock angle for $M_\infty = 5$ with $Kn = 0.07$ agreed fairly well with theory.

The results show that the flow changes significantly as a function of Kn. As Kn increases, the shock thickness and oblique shock angles at the entrance to the channel increase. A new, unexpected result from this study is the behavior of the velocity slip and temperature jump as a function of position along the wall as Kn is varied. We find that the velocity slip and temperature jump at the channel entrance also increase as Kn increases. Moving downstream in any one calculation, the magnitude of the velocity slip is essentially constant, while that of temperature jump gradually decreases.

Acknowledgment

This work was sponsored by the Defense Advanced Research Project Agency and the Office of Naval Research through the U.S. Naval Research Laboratory. We would like to thank J. Ott for providing Navier–Stokes results. The first author thanks the National Research Council for support as a NAS/NRC Research Associate Fellow. The authors also want to thank C.-M. Ho and J. M. McMichael, with whom they have had extensive discussions, and T. X. Nguyen and B. Z. Cybyk for discussions on the SGR and the hypersonic channel flow.

References

[1]O'Connor, L., "MEMS: Microelectromechanical System," *Mechanical Engineering*, Vol. 114, No. 2, 1992, pp. 40–47.

[2]Trimmer, W. S. N., "Microrobots and Micromechanical Systems," *Sensors & Actuators*, Vol. 19, No. 3, 1989, pp. 267–287.

[3]Scott, W. B., "Micro-Machines Hold Promise for Aerospace," *Aviation Week & Space Technology*, Vol. 138, No. 9, 1993, pp. 36–39.

[4]Howe, R. T., Muller, R. S., Gabriel, K. J., and Trimmer, W. S. N., "Silicon Micromechanics: Sensors and Actuators on a Chip," *IEEE Spectrum*, Vol. 27, No. 7, 1990, pp. 29–35.

[5]Liu, J. Q., Tai, Y. C., Pong, K. C., and Ho, C. M., "Micromachined Channel/Pressure Sensor Systems for Micro Flow Studies," *The 7th International Conference on Solid-State Sensors and Actuators, Transducers '93* (Yokohama, Japan), 1993, pp. 995–998.

[6]Pfahler, J., Harley, J., Bau, H., and Zemel, J., "Gas and Liquid Flow in Small Channels," *Symposium on Micromechanical Sensors, Actuators and Systems*, edited by D. Cho, R. Warrington Jr., A. Pisano, H. Bau, C. Friedrich, J. Jara-Almonte, and J. Liburdy, American Society of Mechanical Engineers, DSC 32, New York, 1991, pp. 49–60.

[7]Pong, K. C., Ho, C. M., Liu, J., and Tai, Y. C., "Non-Linear Pressure Distribution in Microchannels," *Application of Microfabrication to Fluid Mechanics*, FED-Vol. 197, New York, 1994, pp. 51–56.

[8]Arkilic, E. B., Breuer, K. S., and Schmidt, M. A., "Gaseous Flow in MicroChannels," *Application of Microfabrication to Fluid Mechanics*, American Society of Mechanical Engineers, New York, FED-Vol. 197, 1994, pp. 57–66.

[9]Bird, G. A., *Molecular Gas Dynamics and the Direct Simulation of Gas Flow*, Clarendon, Oxford, England, UK, 1994.

[10]Bird, G. A., "Application of the Direct Simulation Monte Carlo Method to the Full Shuttle Geometry," AIAA Paper 90-1692, 1990.

[11]Oh, C. K., Oran, E. S., and Cybyk, B. Z., "Microchannel Flow Computed with the DSMC-MLG," AIAA Paper 95-2090, Jan. 1995.

[12]Piekos, E. S., and Breuer, K. S., "DSMC Modeling of Micromechanical Devices," AIAA Paper 95-2089, Jan. 1995.

[13]Cybyk, B. Z., Oran, E. S., Boris, J. P., and Anderson, J. D., "Combining the Monotonic Lagrangian Grid with a Direct Simulation Monte Carlo Model," *Journal of Computational Physics*, Vol. 122, No. 2, 1995, pp. 323–334.

[14]Nguyen, X. N., Oh, C. K., Sinkovits, R. S., Anderson, J. D., and Oran, E. S. "Simulations of High Knudsen Number Flows in a Channel–Wedge Configuration," *AIAA Journal*, Vol. 35, No. 9, pp. 1486–1492.

[15]Oh, C. K., Sinkovits, R. S., Cybyk, B. Z., Oran, E. S., and Boris, J. P., "Parallelization of DSMC Combined with the Monotonic Lagrangian Grid," *AIAA Journal*, Vol. 34, No. 7, 1996, pp. 1363–1370.

[16]Shufflebotham, P. K., Bartel, T. J., and Berney, B., "Experimental Validation of a Direct Simulation by Monte Carlo Molecular Gas Flow Model," *Journal of Vacuum Science Technology B*, Vol. 13, No. 4, 1995, pp. 1862–1866.

[17]Font, G. I., and Boyd, I. D., "Numerical Study of the Effects of Reactor Geometry on a Chlorine Plasma Helicon Etch Reactor," *Journal of Vacuum Science Technology A*, Vol. 15, No. 2, 1997, pp. 313–319.

[18]Yasuhara, M., Nakamura, Y., and Takanaka, J., "Monte Carlo Simulation of Flow into Channel with Sharp Leading Edge," *Rarefield Gas Dynamics: Theoretical and Computational Techniques*, edited by E. P. Muntz, D. P. Weaver, and D. H. Campbell, Vol. 118, Progress in Astronautics and Aeronautics, AIAA, Washington, DC, 1989, pp. 582–596.

[19]Wilmoth, R. G., "Application of a Parallel Direct Simulation Monte Carlo Method to Hypersonic Rarefied Flows," *AIAA Journal*, Vol. 30, No. 10, 1992, pp. 2447–2452.

[20]Vogenitz, F. W., Broadwell, J. E., and Bird, G. A., "Leading Edge Flow by the Monte Carlo Direct Simulation Technique," *AIAA Journal*, Vol. 8, No. 3, 1970, pp. 504–510.

[21]Nance, R. P., Hash, D. B., and Hassan, H. A., "Role of Boundary Conditions in Monte Carlo Simulation of MEMS Devices," AIAA Paper 97-0375, Jan. 1997.

[22]Boris, J. P., "A Vectorized "Near Neighbor" Algorithm of Order N Using a Monotonic Logical Grid," *Journal of Computational Physics*, Vol. 66, No. 1, 1986, pp. 1–20.

[23]Sinkovits, R. S., Boris, J. P., and Oran, E. S., "A Technique for Regularizing the Structure of a Monotonic Lagrangian Grid," *Journal of Computational Physics*, Vol. 108, No. 2, 1993, pp. 368–372.

[24]Phillips, L., Sinkovits, R. S., Oran, E. S., and Boris, J. P., "The Interaction of Shocks and Defects in Lennard-Jones Crystals," *Journal of Physics: Condensed Matter*, Vol. 5, No. 5, 1993, pp. 6357–6376.

[25]Shapiro, A. H., *The Dynamics and Thermodynamics of Compressible Fluid Flow*, Vol. II, Ronald, New York, 1954.

[26]Anderson, J. D., Jr., *Modern Compressible Flow with Historical Perspective*, McGraw–Hill, New York, 1982.

[27]Weber, Y. S., Oran, E. S., Boris, J. P., and Anderson, J. D., "The Numerical Simulation of Shock Bifurcation near the End Wall of a Shock Tube," *Physics of Fluid*, Vol. 7, No. 10, 1995, pp. 2475–2488.

[28]Vincenti, W. G., and Kruger, C. H., *Introduction to Physical Gas Dynamics*, Wiley, New York, 1965.